

HST/WFPC2 Morphologies of K-selected Extremely Red Galaxies

Lin Yan

SIRTF Science Center, MS 220-6, Caltech, Pasadena, CA 91125

lyan@ipac.caltech.edu

David Thompson

The Palomar Observatories, Caltech, Pasadena, CA 91125

djt@iraastro.caltech.edu

ABSTRACT

We selected 115 extremely red objects (EROs) from deep HST WFPC2 archive data combined with ground-based K-band images, with $(F814W - K_s) \geq 4$, K-band SNR ≥ 5 , and a median limiting K_s magnitude of ~ 18.7 , over a corresponding area of 228 sq. arcminutes, for a morphological study of the ERO galaxy population. The survey covered a total of ~ 409 sq. arcminutes over 77 separate WFPC2 fields. This is the first complete sample of bright EROs with high resolution HST morphologies. From a visual morphological classification, we find that $30 \pm 5\%$ of our $(F814W - K_s) \geq 4$ selected sample have morphologies consistent with a pure bulge or bulge-dominated galaxy (equivalent to E/S0), while disks comprise $64 \pm 7\%$ of the sample. Only 6% of the EROs remained unclassifiable. Mergers or strongly interacting systems, which includes sources from both classes, make up $17 \pm 4\%$ of the full sample. The quantitative MDS profile fitting is consistent with these results. These results highlight the complex nature of optical/near-IR color selected EROs. The dominant component of our sample is comprised of disks, not spheroids or strongly interacting systems like HR 10. Using Bruzual & Charlot SED models, we investigated population differences in EROs selected by their $(I - K)$ vs. $(R - K)$ colors and found that I-band based surveys preferentially select systems with prolonged star formation. Real differences in the surface densities of EROs in R -band and I -band based survey may reflect this color selection effect, complicating the comparisons between and interpretations on the nature of the ERO population. We conclude that only a small fraction of EROs at $z \sim 1 - 2$ could be passively evolving ellipticals formed at high redshift through a “monolithic collapse” mechanism. For the majority of EROs, even if most of their stellar mass is already in place at $z \sim 1$, interaction with the environment and accretion of gas still play important roles in their continuing evolution.

Subject headings: galaxies: elliptical – galaxies: fundamental parameters – galaxies: high-redshift – galaxies: spiral

1. Introduction

Extremely Red Objects (EROs), which have optical-to-infrared colors which differ significantly from typical field sources, encompass a wide variety of phenomenæ. Galaxies of assorted types

make up the dominant component of ERO samples, but one can also find low mass stars, gravitationally lensed sources, and transient sources such as variable stars, asteroids or supernovae which may not be initially recognized as such. The term Extremely Red Galaxies (ERGs) is also

commonly used, sometimes interchangeably, but usually refers to a sample of EROs which has been cleaned of the objects which are not galaxies. ERGs are therefore a subset of the EROs. We adopt the more general term ERO throughout this paper.

Both the definition and interpretation of EROs has evolved somewhat since their initial discovery, and it is useful to review the subject here for some historical perspective. When first identified as a distinct population of sources (Elston, Rieke, & Rieke 1988), EROs were thought to be good candidates for primeval galaxies. Subsequent observations (Elston, Rieke, & Rieke 1989), however, showed these early EROs to be $z \sim 0.8$ elliptical galaxies. Additional EROs were noted in the following years (McCarthy, Persson, & West 1992; Eisenhardt & Dickinson 1992; Persson et al. 1993; Graham et al. 1994; Hu & Ridgeway 1994; Soifer et al. 1994; Dey, Spinrad, & Dickinson 1995; Djorgovski et al. 1995; Treu 1998; Im et al. 2002). Most of these were serendipitous detections, identified on images targeting known, high-redshift radio galaxies or other active galactic nuclei. Little or no followup work was done on these objects at the time, which to some extent reflected the limited capabilities of existing instruments and telescopes. These EROs were identified with colors spanning a wide range: $(R - K) \geq 5-7$, or $(I - K) \geq 4-6$.

A resurging interest in EROs accompanied the development of the Submillimeter Common User Bolometer Array (Holland et al. 1999, SCUBA), and the subsequent detection of the extremely red galaxy HR 10 (Hu & Ridgeway 1994, this source is also known as HR94 10 or ERO J164502+4626.4) at $850 \mu\text{m}$ (Cimatti et al. 1998; Dey et al. 1999). At a redshift of 1.44 (Graham & Dey 1996), the detection of HR 10 in the submillimeter implied the presence of massive quantities of dust accompanied by very high star formation rates. The ERO population was thought to provide fertile hunting grounds for more submillimeter-bright galaxies at high redshift. Additional observations have not supported this idea, however, with only a relatively small fraction, on the order of 20% (Andreani et al. 1999; Mohan et al. 2002, Thompson, priv. comm.), of the bright EROs ($K < 19.5$) showing strong submillimeter emission.

The development of larger-format infrared arrays and wider field instrumentation enabled sub-

sequent field surveys to cover enough area to assemble significant samples of systematically selected EROs for further study, in blank fields (Thompson et al. 1999; Daddi et al. 2000; McCarthy et al. 2001) as well as targeted surveys (Chapman, McCarthy, & Persson 2000; Cimatti et al. 2000; Liu et al. 2000). Thompson et al. (1999) adopted a color selection for EROs of $(R - K) > 6^m0$. The motivation was that this color was redder than the expected colors of elliptical galaxies with anything but the highest formation redshifts ($z_f > 10$), and thus represents an extreme color for any normal galaxy. The assumption at the time was that the extremely red galaxy population consisted of either old ellipticals or young, dusty starbursts (Cimatti et al. 1998; Thompson et al. 1999; Dey et al. 1999). The relative contribution of these two types of galaxies would have a bearing on the timing of massive galaxy formation and their subsequent evolution. It is important to emphasize that, at that time, the term “young, dusty starbursts” referred specifically to massive starbursts like that seen in HR 10 or luminous infrared galaxies. Multi-band photometry could potentially distinguish between ellipticals and starbursts (Pozzetti & Mannucci 2000), but this technique requires very low photometric uncertainties to work well (see, for example, Mannucci et al. (2002)).

In order to better study the $z \sim 1$ elliptical galaxy population, Daddi et al. (2000) adopted a bluer color selection limit, $(R - K) > 5.3$, set by the expected colors of a $z = 1$ passively evolving old stellar population. This definition, or the roughly equivalent $(I - K) > 4.0$, for the ERO color selection criterion has generally been adopted in the majority of subsequent work.

While there are a number of redshifts now known for EROs (Graham & Dey 1996; Soifer et al. 1999; Liu et al. 2000; Afonso et al. 2001; Smith et al. 2002b), systematic redshift surveys of complete samples are only now becoming available (Cimatti et al. 2002). Morphological information based on high-resolution HST imaging for complete samples of EROs are also only now starting to appear (Smith et al. 2002a, this work). Without similar spectroscopic or morphological information, earlier ERO surveys divided the ERO population into two components: old, evolved systems or dusty, massive starbursts. But the true

nature of K-selected EROs is likely to be much more complex, as suggested by recent work (McCarthy et al. 2001; Cimatti et al. 2002).

McCarthy et al. (2001) find a large scatter in the $(V - I)$ colors of their ERO sample, best fit by passive evolution models with extended star formation ($\tau = 1$ Gyr). This implies that the star formation history of EROs is more complex than a binary division into evolved ellipticals or dusty, massive starbursts implies. From their K20 survey, Cimatti et al. (2002) found that about half of their spectroscopic sample of ~ 30 EROs are dusty star-forming galaxies with emission lines, while the remaining half are old stellar populations with absorption line spectra. However, the simple presence of line emission could span a wide range of galaxy types, from bulge-dominated, late type spiral galaxies with a small amount of star formation through the more massive starbursts like HR 10. Dust could also completely obscure any on-going star formation, to the point that the optical and UV emission lines are not seen (Poggianti & Wu 2000). Examples of what appear to be quiescent disks at $z \sim 1.5$ exist (van Dokkum & Stanford 2001; Smith et al. 2002b).

There are important differences in the formation and evolution of quiescent normal galaxies and young, dusty, massive starbursts. Morphologies have the potential to distinguish between the various interpretations, which motivated this work.

In this paper, we present the high resolution morphologies derived from HST WFPC2 images for a large sample of K-selected EROs. Our results reveal for the first time a new type of ERO which dominates the population and is neither an early-type galaxy nor a dusty, massive star forming galaxy. We will also discuss the implications of our results for the past and future evolution of massive galaxies at $z \sim 1$.

2. Observations and Reductions

The data used in this survey come from two sources. Deep, high resolution HST/WFPC2 F814W images from archival data, specifically from the Medium Deep Survey (MDS; Griffith et al. (1994); Ratnatunga et al. (1999)), are used for the optical dataset. Images in the K_s band were obtained from the Palomar 60-inch telescope

for a total of 77 MDS fields.

Details on the survey design, observations, reductions and analysis, as well as the details of our visual morphological classification and the automated two-component profile fitting results from the MDS, are given below. In summary, magnitudes were extracted in matched apertures after rotating, rebinning, and convolving the HST data to match the infrared data. A final set of 115 unique EROs satisfying the selection criteria $(F814W - K_s) \geq 4$ and with a K-band signal-to-noise ratio $(SNR) \geq 5$ were identified over a total area of 409 sq. arcminutes. The coordinates, photometry, and morphological classifications for the 115 EROs are listed in Table 2, along with the field name and source identification from the Medium Deep Survey.

2.1. Field Selection

Our target fields were selected from the MDS database to have a 5σ sensitivity of $F814W \geq 24^m$ (Vega), which would provide a good signal-to-noise ratio (SNR), high resolution optical image for morphological classifications for the majority of the EROs we might detect. This corresponds to a minimum total exposure time of ≥ 2700 s, typically split over 2 or more exposures to aid in the removal of cosmic rays. We restricted the target fields to high Galactic latitudes, $b_{II} \geq 20^\circ$, to minimize foreground stellar contamination, and make no explicit corrections for Galactic extinction. For most fields, the color correction is under 0^m1 . Finally, we selected primarily northern hemisphere fields ($\delta \geq -15^\circ$) to preserve accessibility from Palomar Observatory.

The fields were selected without regard to any specific science targets. The majority of the MDS database is composed of random parallel fields imaged while the primary science target was observed in another HST instrument. However, there are a significant number of fields containing known clusters present in the MDS database, twelve of which we imaged as part of this survey. Gravitational lensing from these foreground clusters (typically at redshifts of a few tenths) can boost the observability of faint EROs. This technique has been used with success in surveys targeting EROs (Smith et al. 2002a), submillimeter-bright galaxies (Smail et al. 1999), and other high redshift sources (Ellis et al. 2001). We note here

that any lensing will be unbiased with respect to galaxy morphologies, and so we make no specific corrections for lensing from cluster fields observed in this survey. Lensing can, however, boost the surface densities of EROs (see §3.2). We note that there is no overlap in target fields between our survey and that of Smith et al. (2002a).

2.2. WFPC2 F814W Images

We retrieved the F814W images from the MDS database at Space Telescope Science Institute (see <http://archive.stsci.edu/mds/cdrom.html>). These data have been processed through the MDS data reduction pipeline, which includes warm pixel correction, image stacking, removal of cosmic rays, and photometric calibration. For a complete description of the MDS reduction pipeline, see Ratnatunga et al. (1999). In general, this automated reprocessing produces the best results on fields where multiple ($n > 3$), dithered images were obtained, and where the field and its immediate surroundings are free of bright stars. These processed images are stored in the MDS database in the HST standard GEIS format, where each of the 4 CCDs and their associated header information is stored in a separate layer of the disk file.

For each of our target fields, we retrieved these GEIS format images, then processed them further to meet the needs of our survey. The data were processed using standard IRAF¹ tasks, plus specialized routines developed for WFPC data found in the STSDAS package.

First, we interpolated over bad pixels flagged by the MDS processing, subtracted the background, and corrected any additional deviant pixels identified by the COSMICRAY routine. The STSDAS task WMOSAIC was used to correct for distortion in the WFPC2 images and assemble the data from the four separate CCDs into a single mosaic image. This additional processing does miss some cosmic rays, but any contamination of the EROs is minimal, and only serves to make the sources bluer than they would otherwise be.

¹IRAF is distributed by the National Optical Astronomy Observatories, which are operated by the Association of Universities for Research in Astronomy, Inc., under cooperative agreement with the National Science Foundation.

2.3. K-band Imaging

Ground-based K_s images were obtained using the near-IR camera on the Palomar 60 inch telescope (Murphy et al. 1995). The camera has a $160'' \times 160''$ field of view, well-matched to WFPC2. The detector is a 256^2 pixel HgCdTe, covering $0''.62$ per pixel. A total of 42 nights went into this project, spanning the time period of 2000 August 11 – 2001 June 06 UT. Useful data was collected on 21 photometric nights. We imaged 77 MDS fields under photometric conditions, with repeat observations on about one-third of the fields to help determine the photometric uncertainties. The repeat observations show less than $0''.1$ of systematic variations. We targeted exposure times of 75 minutes (4500 seconds) per field, which yields a 5σ point-source sensitivity of $K_s \sim 18^m.75$ in good seeing.

The data were reduced following standard infrared reduction procedures. Each frame was sky-subtracted with temporally-adjacent images and then flatfielded with a combination of dome and twilight sky flats. Offsets were determined from as many sources as possible (with a minimum of one, as the header coordinates were insufficiently accurate to stack the data with confidence). A bad pixel mask was used to reject dead or excessively hot pixels, and the data combined with integer pixel offsets into the final mosaics for each field.

Observations of the Persson infrared photometric standards (Persson et al 1996) were obtained throughout the night, and used to derive the zero points and airmass corrections. For the photometric data, the zero points show only 0.02 mag rms variations from night to night. This is added into the photometric uncertainties of individual objects in quadrature.

The 5σ sensitivities in the centers of the infrared mosaics ranges from $18^m.2 - 19^m.5$. This was calculated from the per-pixel sky noise at the center of the infrared mosaics, and scaled to an aperture diameter equal to 2.5 times the FWHM of the seeing. The seeing ranges from $1''.2$ to $2''.5$, with the majority of the data better than $1''.8$ (3 pixels FWHM). The lower sensitivities are generally due to poorer seeing conditions, while the deeper data are from stacking observations from multiple nights. A summary of the useful observations are given in Table 1, which lists the field,

exposure times for both the K_s and F814W images, and the central 5σ K_s sensitivity.

2.4. Matched Aperture Photometry

The original full resolution F814W images were rotated, rebinned and convolved to match the infrared image orientation, scale and seeing. The optical and infrared images were then co-aligned and cropped to matching areas on the sky. The resulting image pairs were used for extraction of the photometry. A set of IRAF scripts were written to speed the execution of these and subsequent tasks in creating the final photometric catalogs.

Because the K-band image mosaics have increasing noise at the edges, source detection was performed on a noise normalized image so that a uniform detection threshold could be applied. The noise normalization was done by multiplying the K-band image mosaic by the square root of an exposure time map. We used the Source Extractor software (Bertin & Arnouts 1996) for the initial source detection on the K-band data. However, uncorrected distortions and/or small residual offsets between the image pairs ultimately required recentering on objects in the scaled and seeing-convolved HST data. Re-centering of the photometric apertures on the HST data was reviewed interactively for all sources with initial colors greater than $(F814W - K_s) > 3^m8$, as illustrated in Figure 1. This review process also allowed for rejection of spurious sources from the photometric catalog, as well as noting the effects of uncorrected cosmic rays or contamination from nearby galaxies. Note the complete lack of morphological information in the ground-based imaging, while the full-resolution image clearly shows a galaxy with a disk.

The final aperture photometry was extracted using the APPHOT package in IRAF. We adopted an aperture diameter of 2.5 times the seeing FWHM of the corresponding K-band image. This represents a compromise between a larger aperture, which yields a fairer measurement of a galaxy's total magnitude as well as provides a better measure for intrinsically large galaxies, and a smaller aperture, which would minimize contamination from other sources close to the line-of-sight to the ERO. The majority of the K-band data are better than $1''.8$ FWHM (3 pixels), so the photometry was extracted in apertures typically smaller

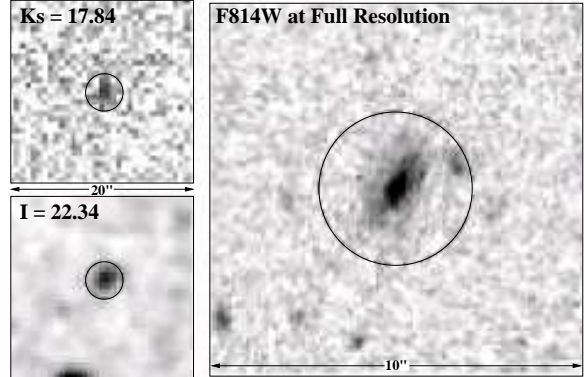


Fig. 1.— An example from the aperture photometry review process. The photometric images, with the HST data rebinned and convolved to match the infrared data, are shown in the two panels to the left. The larger image to the right shows the full-resolution WFPC2 data. The circles in all three panels are scaled to the size of the aperture used for photometry (here, $4''.2$ diameter).

than $4''.5$ in diameter. Because the K-band images have non-uniform noise and depth, the SNR for each galaxy was determined locally. For faint objects, the SNR is dominated by the sky noise within the photometric aperture.

In 20% of the cases, the photometric apertures do include close companions which could affect the F814W photometry. This has the effect of making our measured colors for these objects bluer than the true color of the ERO, and thus a lower limit. We were able to correct for the majority of contamination problems during the review process, but we note that the presence of companions should not be biased toward any particular morphological type.

2.5. Survey Area

Because our survey is composed of many separate images obtained on different nights, under different seeing conditions, and with different exposure times, the depth of each field varies. Also, since the infrared camera field size is only slightly larger than the HST WFPC2 mosaic, and given the random orientations for the HST data, portions of the HST images often overlap the higher-noise area around the edges of the infrared mosaics. These factors combine to make the total

survey area a function of the depth, while allowing maximal use of the survey data.

We integrated the survey area as a function of magnitude on a per pixel basis. Ideally, this should be done over resolution elements. However, aside from single-pixel deviations due to masked bad pixels or cosmic rays, the depth in the infrared data only changes relatively slowly with position around the edges.

To sum the survey area, we first created a mask for the co-aligned images covering the area on the sky outside the borders of the WFPC2 data. An effective exposure time map for the infrared mosaic was then converted into a map of the limiting magnitude in each pixel as:

$$m_{pix} = m_{lim,cent} + 2.5 \log(t_{pix}/t_{max})^{0.5}$$

where t_{pix} is the exposure time that went into the individual pixels in the final infrared mosaic, and t_{max} is the total exposure time for that image.

A histogram of the unmasked pixel limiting magnitudes (pixels also covered by the HST data) was then created for each survey image in $0^m.1$ bins. The resulting 77 histograms were combined, and scaled by the area per pixel. This differential area histogram was finally integrated from the faint to the bright limits. A plot of the integrated area as a function of the limiting magnitude is shown in Figure 2. The full survey area is 409 square arcmin, with more than half of this (228 sq. arcmin) reaching to at least a depth of $K_s = 18^m.75$.

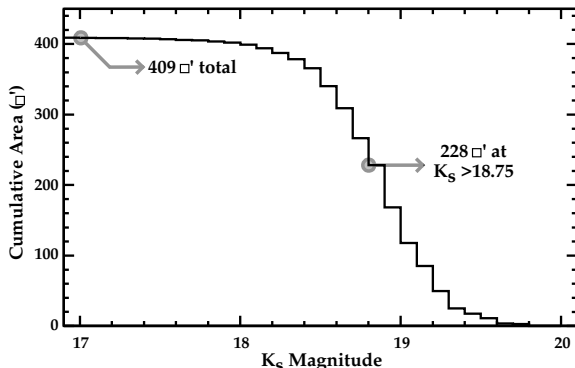


Fig. 2.— Area covered by this survey as a function of the K_s magnitude. Half of the total area was surveyed to at least $K_s = 18^m.75$ in depth.

2.6. The ERO Sample

A total of 115 unique galaxies satisfy the selection criteria of $(F814W - K_s) \geq 4$ and with a K-band signal-to-noise ratio (SNR) ≥ 5 , were selected over a total area of 409 sq. arcminutes. The coordinates, photometry, and morphological classifications for these 115 EROs are listed in Table 2, along with the field name and source numerical identification from the Medium Deep Survey. We show the combined color-magnitude diagram for all 77 fields in Figure 3. All independent observations are included, so some sources are plotted more than once. In Figure 4 we detail the photometric uncertainties on the ERO sample.

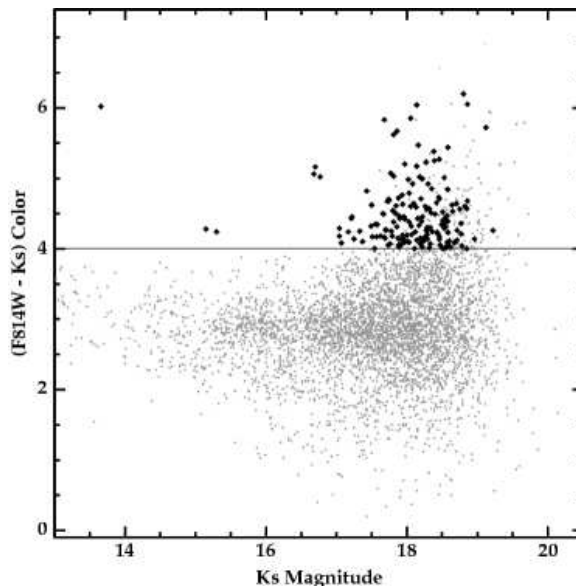


Fig. 3.— The full color-magnitude diagram for this survey. All points are plotted, including duplicate observations of the same source on two or more nights. Sources satisfying the color selection of $(F814W - K_s) \geq 4$, and with a K-band SNR ≥ 5 , are plotted with heavier symbols.

Not included in Table 2 are six sources which were obvious stars, most of which were not intrinsically red but simply saturated on the HST images. We also excluded the gravitationally lensed system MG 0414+0534 (Lawrence et al. 1995), which does satisfy the adopted selection criteria, but was the science target for the HST observations and thus was not a randomly selected source.

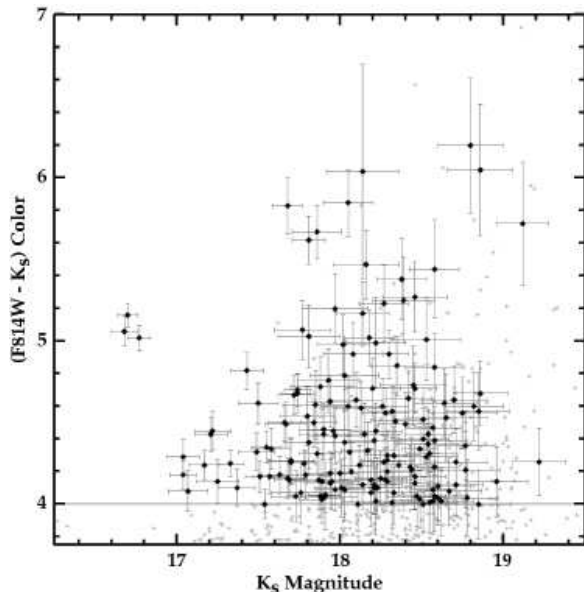


Fig. 4.— A higher resolution plot of the color-magnitude diagram shown in Figure 3, covering the region where EROs were selected. Photometric uncertainties for the EROs are also plotted. Note that there are a number of sources which are redder than the color selection limit, but which were not kept in the ERO sample. Most often, this was due to a low SNR in the K-band image.

2.7. Morphological Classification

The main goal of this survey is to utilize the high resolution WFPC2 images to study the morphological properties of EROs. We classified the sources visually, but also compare our results to the automated profile fitting from the MDS. The details are described below.

The full-resolution HST/WFPC2 images of all of the EROs in our sample are shown in Figure 10. The authors strongly caution the reader against attempting to morphologically classify the EROs solely from these grayscale images. The HST data are freely available from STScI, and interested readers are encouraged to retrieve the original data.

2.8. Visual Classification

Visual morphological classification on nearby galaxies has had a significant impact on our understanding of galaxy formation, environment, and

evolution. However, it is widely acknowledged that visual classification is an inherently uncertain and subjective process. In the high redshift regime, the visual classification of galaxy morphology is further complicated by limited resolution (even with HST), lower SNR, $(1+z)^4$ cosmological dimming, and observations at restframe wavelengths which vary with the redshift. Several detailed studies on the biases in visual morphological classifications of high redshift galaxies have been made (Hibbard & Vacca 1997; Odewahn et al. 1996). Despite its inherent uncertainties and subjectiveness, visual morphological classification has proved to be a powerful tool for galaxies at $z \sim 1$, as demonstrated by many studies using deep HST images in the HDF, as well as morphological studies of galaxies in high-redshift clusters (Lubin et al. 1998; Dressler et al. 1997; Couch et al. 1998; Smail et al. 1998). One important point illustrated in these empirical studies, and also in simulations (Hibbard & Vacca 1997), is that the extended morphological features remain readily visible in deep HST F814W images out to $z \sim 1$. In light of this, we have visually classified all the EROs in our sample.

Because of the bright K_s magnitude limits in this survey, all 115 galaxies in our sample are detected in the F814W images, most well resolved and with a high SNR. As a training set for our visual classification, we examined in detail the F814W images from the MDS database for *all* of the galaxies in $z = 0.9$ cluster CL1603+4304, which is one of the target fields included in this work (u2845). Most of the cluster members are much brighter than the EROs. Since the cluster is quite distant, the cluster members have similar apparent sizes and suffer from similar cosmological dimming as the EROs. Morphological classifications for these galaxies were published in Lubin et al. (1998). Working down the full range of apparent magnitudes, it was increasingly difficult to classify the fainter galaxies into the traditional galaxy morphological types (Elliptical, S0, Sa/Sb/Sc Spirals, Irregulars), although it was still possible to distinguish between spheroidal systems (presumably mostly elliptical and S0 galaxies) and disk systems (Sb/Sc/Irr). Spirals of type Sa represent a somewhat fuzzy boundary. Depending on the SNR or strength of any ongoing star formation, these could be classified either way. We therefore

opted to simplify our morphological classification of the EROs.

We visually classified the galaxy morphologies into four broad categories. These categories were selected to parallel the MDS classifications, as well as reflect the difficulties in placing faint, high-redshift sources into the traditional morphological classes, however there are close parallels between the two systems. EROs classified as spheroids or pure bulge galaxies (B) show no convincing evidence for the presence of a disk. Bulge-dominated (BD) systems show evidence of a disk, but the majority of the luminosity is coming from the spheroidal component, and any disk component is generally featureless. Disky systems with some evidence of a bulge (DB) generally show some evidence for structure in the disk (e.g. spiral arms or dust features), and the luminosity is not generally dominated by the spheroidal component. Finally, disks (D) do not show any obvious bulge component, and often have mottling or other structure visible in the disk. Some sources were too low of a SNR to classify, so they were listed as unclassifiable (U). We further noted whether the ERO appeared to be undergoing a strong merger or interaction with other nearby galaxies regardless of their color.

All of the EROs in our HST images were classified independently on a video display by both authors. We then combined the classifications and reviewed the sources together to resolve the disagreements, which involved $\sim 20\%$ of the sample, and to settle on a final classification. We also reviewed the EROs grouped into their separate categories. This review involved looking at our reprocessed images as well as the MDS pipeline-processed images.

2.9. MDS Profile Fitting

For a more quantitative analysis of the galaxy properties, we utilized the galaxy profile fitting results from the MDS database. For almost all of our EROs, the MDS database includes a set of morphological parameters derived from their automated object detection and classification algorithms. More detailed information on the entire MDS reduction pipeline and morphological classification process can be found in Ratnatunga et al. (1994) and Ratnatunga et al. (1999), as well on the MDS website at

<http://astro.phys.cmu.edu/mds.html>.

The MDS automated object classification involved a two-dimensional maximum likelihood estimator (MLE) analysis that automatically optimizes the model and the number of parameters to be fitted to each object image. Two scale-free, axisymmetric models are chosen to describe the galaxy profile. The spheroidal component, which would include elliptical galaxies and the bulges of spirals, is assumed to follow a de Vaucouleurs profile, while the extended disk component follows an exponential profile. Each profile is characterized by a major axis half-light radius and axis ratio. Point-like stellar sources are examined through the same procedure, except that a Gaussian profile is used. A maximum likelihood parameter estimation is used to determine the best model and the parameter values. For each set of model parameters, a model image of the object is created and compared with the actual object images. Finally, a best-fit model and its parameters are classified with the following categories for resolved sources: bulge, bulge+disk, disk, and galaxy (generally for low SNR sources where neither a bulge nor disk classification is significant). We use the model bulge to total luminosity ratio to divide bulge+disk galaxies into our classes BD (for $L_B/L_{Total} \geq 0.5$) and DB. This method does not classify irregulars, mergers, or interacting systems as such.

2.10. Comparison of Classifications

Figure 5 shows a comparison of the visual and MDS classification results for EROs classified by both methods. We group the B and BD classes under the label “spheroids” and the DB and D classes under the label “disks.” The darker gray areas show where the two methods agree reasonably well, while the lighter gray areas show the disagreements. Overall, the agreement is good, where both the “spheroids” and “disks.” in the two classification methods agree at the 70% level. The largest source of disagreement comes from EROs which were visually classified as DB (disk with a bulge), but which the MDS classified as a pure bulge. A majority of these systems are relatively faint in the HST images, where it can be difficult to distinguish between an extended spheroid or a disk, but also acknowledge the possibility of a fundamental failure in properly classifying sources vi-

sually. Most of the remaining disagreement stems from the split between BD and DB, and can be tuned out by modifying the division in the MDS bulge-to-total luminosity ratio from the arbitrary 50% bulge-to-total adopted for this study.

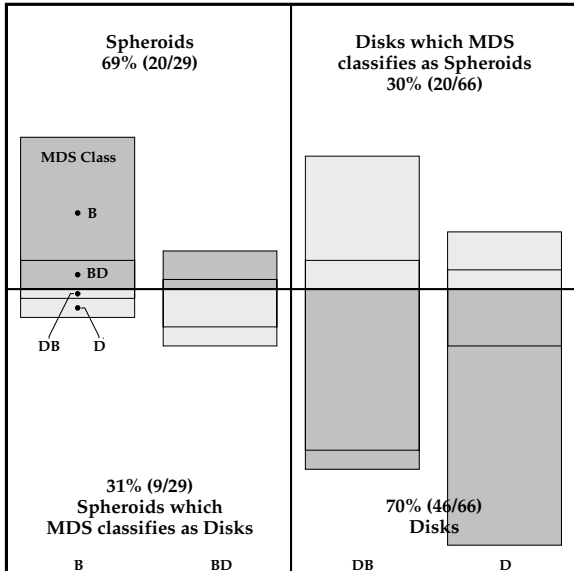


Fig. 5.— Cross comparison of the visual and MDS morphological classification results. The darker gray areas are where the two methods agree well. Overall, there is a 70% agreement in the broad division of EROs into “spheroids” or “disks.”

3. Results & Discussion

3.1. Morphological Distribution

Our morphologies are based on F814W images. Assuming the median redshift of one for EROs from the Cimatti et al. (2002) sample with $K \leq 19.2$, the WFPC2 data sample a rest-frame wavelength of 4100 Å. The F814W images thus represent a compromise between sensitivity to star formation at shorter restframe wavelengths and better probing any extended old stellar populations at longer restframe wavelengths. As shown in simulations by Hibbard & Vacca (1997), morphological classifications using F814W images do not show any significant biases at $z \sim 1$.

Using the results from our visual classification, we find that $30 \pm 5\%$ of our EROs have morphologies consistent with spheroidal (B and BD) galax-

ies. Disks (D and DB) dominate the EROs at $64 \pm 7\%$ of the sample. Only 6% of the EROs were unclassifiable, due primarily to low SNR on the WFPC images. The uncertainties are derived simply from the square root of the number of EROs in that subset, and does not try to include the unclassifiable sources. We plot in Figure 6 the relative fractions of spheroids and disks in our visual classification as well as from the MDS profile fitting.

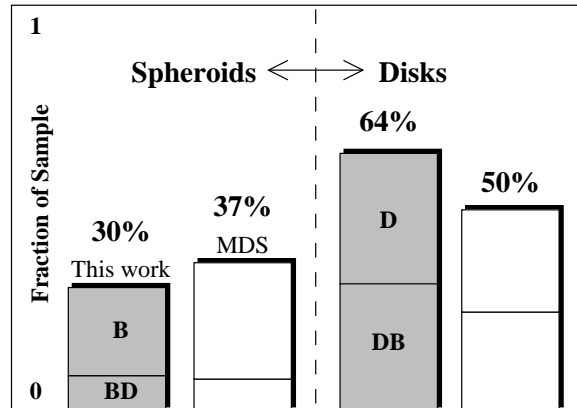


Fig. 6.— Relative fraction of spheroidal galaxies vs. disks as classified in this survey (gray bars) and by the MDS automated profile fitting (white bars). Not included in this plot are the 6% of sources unclassifiable by us or the 14% unclassified by the MDS.

We find that the relative morphological mix of EROs in subsets constructed of the EROs in known foreground galaxy cluster fields vs. those selected in the remaining “blank” fields is consistent to within the uncertainties. Since any lensing should be unbiased with respect to background galaxy morphologies, we do not differentiate between cluster and field sources in the remaining analysis.

Some of the EROs, including both disks and spheroids, appear to be involved in recent mergers or show evidence of strong interactions (e.g. tidal tails, strong asymmetries). These comprise $17 \pm 4\%$ of the sample. Without additional information, these systems represent the most likely source of possible large-scale starbursts. This is consistent with the observation that among *bright* EROs, roughly 20% have $850\mu\text{m}$ detections (Andreani et al. 1999). One third of the galaxies we

classed as spheroids have one or more faint companions or show signs of recent interaction, suggesting that a significant fraction of otherwise old stellar populations may not be in purely passively evolving systems.

The morphological classifications derived from the MDS profile fitting are largely consistent with our visual results, but show a slightly higher fraction of spheroidal galaxies, with $37 \pm 6\%$ of the sample classed as B or BD (with a bulge fraction larger than 50%). There is a corresponding drop in the disk fraction, with $50 \pm 7\%$ classed as DB or D, but disks still dominate the overall $(I - K) \geq 4$ ERO population. A larger fraction of the sample, $14 \pm 3\%$, were not fit with the bulge+disk models due to low SNR or a more conservative avoidance of the CCD edges in the WFPC2 data.

We find that our ERO sample selected with $(F814W - K_s) \geq 4$ is dominated by disk galaxies, and not by spheroids or strongly interacting systems. The star formation rates in these disks could span a wide range, including normal galaxies with fairly quiescent star formation. HR 10 type systems, with mostly young stars and undergoing massive starbursts, may comprise only a small fraction of the sample. The origins of their red colors may be traced to a significant old stellar population combined with some dust extinction, especially considering the edge-on orientation of many of the disks in our sample of EROs. Even though most of the stellar mass may already be in place by $z \sim 1 - 2$ for these EROs, such a large fraction of disk galaxies implies that there is still a substantial amount of gas available to feed ongoing star formation.

The existence of such a large fraction of disk galaxies and interacting systems in our sample suggests that hierarchical merging may be an important mechanism for the formation and evolution of the ERO population. However, the scenario in which ellipticals were formed in a “monolithic collapse” at high redshifts and evolve passively thereafter cannot be excluded. While 30% of our ERO sample are clearly early type galaxies, whose colors are consistent with old stellar populations formed at high redshifts. We also found that one-third of the spheroids in our sample have faint companions or signs of interaction. This suggests that although a majority of their mass could be assembled rapidly at high redshift, these systems

are not simply isolated, passively evolving old stellar populations, and continuing accretion of gas or merger events plays a significant role in their evolution. Examples of secondary star formation in field E/S0s ($z \sim 0.1 - 0.73$) can be found in Treu (2002).

Our results contradict those of Moriondo, Cimatti & Daddi (2000), which are also based on HST morphologies. They find that 50–80% of their sample have E/S0 morphologies on the basis of one-component exponential model fits. However, we note that their ERO sample was assembled from the published literature, with the corresponding heterogeneous selection functions of the original surveys. In addition, the morphologies were determined on HST images from both WFPC2 and NICMOS, probing widely different rest-frame wavelengths and thus differing sensitivities to star formation or old stellar population.

3.2. Surface Density

The integrated surface density of EROs, is defined as total number of EROs brighter than a given magnitude per unit area on the sky. Because the area covered in this survey is a function of the magnitude, the differential number of EROs selected in each magnitude bin is a function of both the magnitude and the area surveyed. Calculating the integrated surface density thus required rescaling the number of EROs in each of the brighter bins by the appropriate area ratio prior to integration. We plot the resulting surface density of EROs from our survey derived by this method in Figure 7 (filled diamonds). The uncertainties were derived simply from the square root of the rescaled number of EROs.

For comparison, we also plot in Figure 7 the results from other recent surveys (Thompson et al. 1999; Smith et al. 2002a; Daddi et al. 2000; McCarthy et al. 2001; Cimatti et al. 2002; Barger et al. 1999). The primary difficulty in making such comparisons is that each survey used a different set of filters and different selection criteria for identifying EROs. In order to make a general comparison between these disparate surveys, we make several simplifying assumptions. First, we treat all K filters as functionally equivalent (e.g. $K = K' = K_s$), so no color terms are applied to convert magnitudes between them. The same is true for the several different I filters and

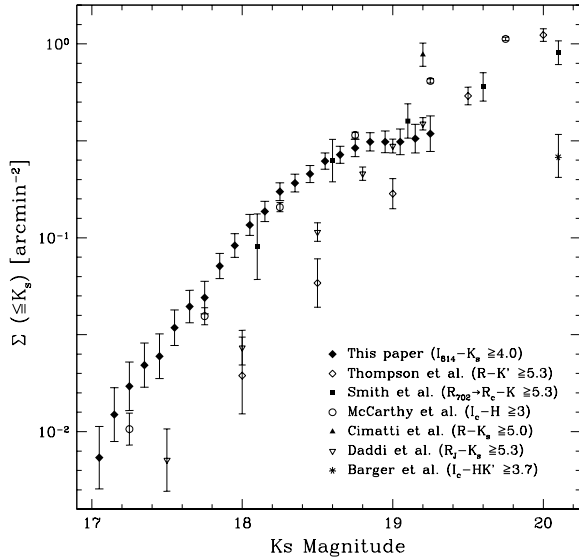


Fig. 7.— Cumulative ERO surface density from this work (filled diamonds), as well as several other surveys for comparison. The uncertainties are derived assuming only Poisson counting statistics in each bin.

R filters used. We note that these assumptions are generally made in most recent published ERO surveys unless the color selection limit is explicitly tied to some fiducial model SED, typically a passively evolving $z = 1$ old stellar population (i.e. elliptical galaxies), *and* the specific filters used for the survey. Second, we adopt the generic colors of $(R-I)=1^m3$ and $(H-K)=1^m0$ to convert the surveys based on R band or H band data to our $I-K$ colors. Third, we plot without additional correction the Cimatti et al. (2002) results, even though they select EROs at a bluer limit: $(R-K_s) \geq 5^m0$. Finally, we adopt the Barger et al. (1999) results directly for $(I_c - HK') \geq 3^m7$, which they show to be equivalent to $(I-K) \geq 4^m0$ for that filter set.

While the generic color conversions we adopt obviate the possibility of more detailed comparisons between the different ERO surveys, they do allow us to consider broad trends in the surface densities as a function of the selection filters. First, the two I-band based surveys (this work and McCarthy et al. (2001)) agree quite well over the region $17^m \leq K_s \leq 19^m$. This suggests that our sample is neither significantly inhomogeneous nor incomplete over this range, although the turnover

in counts to fainter magnitudes suggests incompleteness in our sample for $K > 19^m$. The two larger R-band based surveys (Thompson et al. 1999; Daddi et al. 2000) also agree with each other over this same range in K-band magnitude, but are systematically about a factor of three lower than the I-band surveys. The lensing-corrected surface density of EROs from the cluster-pointed survey of Smith et al. (2002a), despite using an R-band filter, agrees well with the I-band based surveys at brighter magnitudes ($K < 19^m$). The other two surveys, Cimatti et al. (2002); Barger et al. (1999), differ from the other results.

Aside from the uncertainties in converting from one filter system to another, there are two primary effects which can qualitatively account for the similarities and differences in the surface densities of EROs from these different surveys: cosmic variance, and color selection effects. Both the Cimatti et al. (2002) and Barger et al. (1999) surveys cover relatively small, connected areas on the sky, and are thus more subject to cosmic variance, especially considering the strong clustering seen in Daddi et al. (2000). The Smith et al. (2002a) survey is composed of 10 widely-separated sight lines and thus should be less sensitive to cosmic variance, but their sample does show a wide field-to-field variation in the number of EROs. Cimatti et al. (2002) selects EROs at a bluer limit, $(R-K_s) \geq 5^m0$, which likely contributes to their higher ERO surface density.

A color selection effect may contribute to the apparent differences in surface density between R-band based (Thompson et al. 1999; Daddi et al. 2000) and I-band based (this work and McCarthy et al. (2001)) ERO surveys. We offer below (see §3.5) a qualitative argument on this, as we do not have a proper multiband deep survey to address this with real data.

3.3. Volume Density

We can make an estimate of the volume density of EROs with some assumptions on the range of redshifts at which they may be found, and compare these results with the local density of massive galaxies. The color selection limit of $(I-K) \geq 4^m0$ sets the lower redshift bound to $z = 1$, which is appropriate for passively evolving old stellar populations. However, photometric uncertainties could make this $z = 1$ boundary somewhat fuzzy. Galax-

ies with significant dust extinction (see the following section) could also lie at lower redshifts. Cimatti et al. (2002) obtained spectroscopic redshifts for a sample of EROs with $(R-K) > 5$ which includes sources of both types down to $z \sim 0.7$. We adopt an upper cutoff to the assumed redshift range of $z = 2$, as higher redshift EROs would be anomalously luminous given their bright K -band magnitudes.

Under the above assumptions, we derive a co-moving volume covered by our survey to be $4 \times 10^5 h_{70}^{-3} \text{ Mpc}^3$. This volume is only weakly dependent on the assumed redshift range, and only changes by a factor of two if the redshift range is narrowed to $z \sim 1.0 - 1.5$ or broadened to $z \sim 0.7 - 2.8$. This volume was derived from the total survey area of 409 square arcminutes, and does not take into account the variable survey depth with magnitude.

The galaxies classed as spheroids in our survey have a co-moving volume density of $1 \times 10^{-4} h_{70}^3 \text{ Mpc}^{-3}$. The disks have a co-moving volume density about twice as large, and the total ERO sample (115 EROs) reach a density of $3 \times 10^{-4} h_{70}^3 \text{ Mpc}^{-3}$.

To compare with nearby massive galaxies, we adopt the local K -band luminosity functions from Kochanek et al. (2001). We integrate from $10L^*$ down to $1L^*$, which corresponds to our K -band limit at $z = 1$ after correcting for passive evolution and cosmological K -corrections. We find that the EROs can account for only one-third of the local massive galaxies, and that the relative morphological mix is about the same in the two samples. This is reasonable, but should be considered only an order-of-magnitude agreement given the factors of ~ 2 uncertainties in the volume densities arising from the assumptions on the redshift distributions, area surveyed as a function of depth (§2.5), and contamination (§3.4).

3.4. Dust Extinction in Disky EROs

While classifying the EROs, we also noted that 40% of the disk systems (DB and D) appeared to be sufficiently edge-on that even small amounts of dust in a disk could have a disproportionately large effect on the overall system color. These systems are noted in Table 2 with italicized entries

under morphology: *DB* and *D*, and we show two examples of edge-on EROs in Figure 8. This is far more than expected from a set of randomly oriented galaxies, suggesting that orientation effects are responsible for their inclusion in the ERO sample.

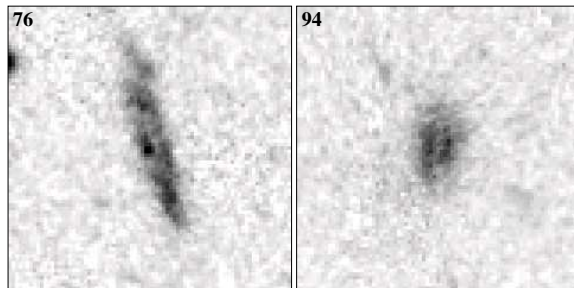


Fig. 8.— Examples of two edge-on disks where dust extinction may contribute significantly to their overall $(I - K_s)$ color. Each image is $8''$ square. The labels correspond to their source numbers from Table 2.

Given the potentially large extinctions possible from dust in otherwise normal disk galaxies, it is possible that the edge-on systems are at lower redshift ($z < 1$). Several of these show extended disks of large apparent size (several arcseconds), which would be unusually large (tens of kiloparsecs) if at $z \sim 1$ or more. The edge-on systems comprise half of the disk EROs, or one-third of the total $(I - K)$ selected ERO sample. They thus represent a large and previously unanticipated source of contamination in the ERO population.

3.5. Color Selection Effects

How comparable are ERO samples selected using an $(R - K) \geq 5.3$ color versus an $(I - K) \geq 4$ color? This important issue has never been clearly addressed. We investigated this issue using model spectral energy distributions, but lack the necessary multiband data to compare to the models. Deep, wide-field infrared/optical surveys should be able to address this point in more detail.

In Figure 9 we plot the $(R - K)$ vs. $(I - K)$ colors for a Bruzual & Charlot (1996) model approximating an old stellar population (OSP, $\tau = 0.1, z_f = 30$) or passively evolving elliptical galaxy. We also plot two models with longer exponential decay times ($\tau = 1.0$) but differing for-

mation redshifts ($z_f = 30, 5$), which should contain a significant fraction of old stars in the range of $1 < z < 2$, but still have some residual star formation. A similar plot covering the VIH color-color plane can be found in (McCarthy et al. 2001, their Figure 2). Their data show that EROs selected with $(I - H) \geq 3$ have a wide scatter in the $(V - I)$ color, which the authors interpreted as due to prolonged star formation.

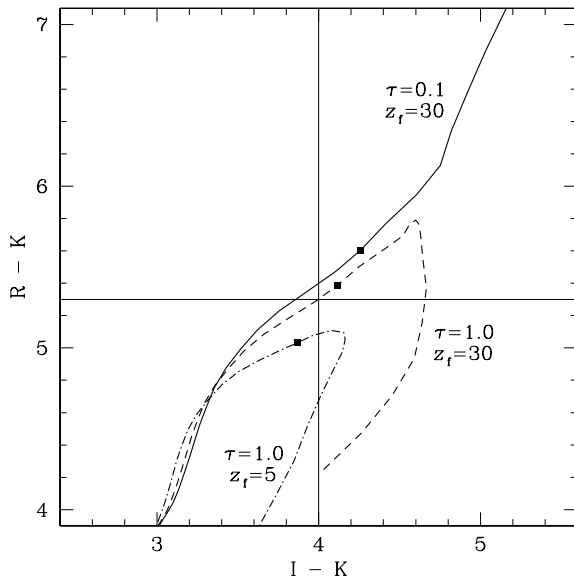


Fig. 9.— RIK colors for a Bruzual & Charlot (1996) model approximating an old stellar population (OSP, $\tau = 0.1$, $z_f = 30$), as well as two models with longer exponential decay times ($\tau = 1.0$) but differing formation redshifts ($z_f = 30, 5$). All three curves are marked with squares at $z \sim 1$. Note that that pure, passively-evolving OSPs would be selected in either an $(R - K)$ or $(I - K)$ survey for EROs, but that any residual star formation, such as from a disk, would quickly drop objects out of the $(R - K)$ sample. Reducing the redshift of formation much below five, or increasing the residual star formation rates ($\tau > 1$) would drop objects out of both samples. Dust counteracts these effects somewhat, shifting objects towards the upper right of this plot.

The two dotted lines in Figure 9 mark the fiducial colors $(R - K) = 5^m3$ and $(I - K) = 4^m0$, representing the colors of a $z = 1$ passively-evolving elliptical galaxy used by most surveys to select EROs. The squares mark the $z \sim 1$ points in each

model curve. Assumptions on the models used, as well as the assumed cosmology and the specific filter bandpasses used for ERO surveys can account for several tenths of a magnitude variation in the expected colors of a $z = 1$ passively-evolving elliptical galaxy.

Several predictions can be made from this color selection effect. First, is that both R-band and I-band based ERO surveys should select the *same population* of passively-evolving old stellar populations (elliptical galaxies). Second, I-band based ERO surveys should preferentially include disk galaxies. Light from a bulge comprised of older stars would dominate the $(I - K)$ color, while even small amounts of residual star formation in the disk keeps them too blue in $(R - I)$ to be included in an $(R - K)$ selected sample. Other factors, such as dust extinction, may counteract the star-formation and contribute significantly to their overall color. This implies that ERO samples selected on their $(R - K)$ color may not be comparable to samples selected on their $(I - K)$ color.

Figure 9 can also be used to set some constraints on the formation redshift for the EROs. Models with exponential decay times longer than about 1.5 Gyr ($\tau \geq 1.5$), or with a formation redshift lower than five ($z \leq 5$) simply have too much residual star formation. Without any reddening from dust, the blue light from a young population of stars would be sufficient to drop these galaxies out of either $(R - K)$ or $(I - K)$ samples of EROs. Thus, the brighter EROs classed as spheroids, especially those without any evidence of a disk or ongoing star formation, are likely to have formed a majority of their stars at relatively high redshift ($z > 5$).

The morphological mix in our sample of relatively bright, $(I - K)$ -selected EROs is similar to that of Smith et al. (2002a) among a sample of fainter EROs ($K \leq 20.6$, $R - K \geq 5.3$) identified in the fields of foreground clusters massive enough to gravitationally lens the higher redshift EROs. They classify 18% of their sample as compact, and 50% as irregulars (including disk-like systems), while 32% are too faint to be classified.

Considering redder subsamples from both this work ($F814W - K_s \geq 5$) and Smith et al. (2002a) ($R - K \geq 6.0$), we again find similar results. Of the 11 redder EROs in our sample, nine were clas-

sifiable. Of these nine, $89 \pm 31\%$ have disk morphologies, a much higher fraction than in the full sample. The redder Smith et al. (2002a) subsample has $\sim 90\%$ with disk/irregular morphologies.

The expectation from the color selection effect is that (R-K) samples should contain a higher fraction of spheroids at a given K magnitude limit. However, the fainter Smith et al. (2002a) sample, about three magnitudes deeper than our ERO sample, is composed primarily of irregulars and disks. This suggests that the morphological mix of EROs does change at fainter magnitudes, and Smith et al. (2002a) conclusion that fainter and redder samples are dominated by massive, dusty starbursts does not contradict our findings. Clearly, this color selection effect needs to be investigated further, with larger and deeper samples of EROs with both (R-K) and (I-K) selection on the same area of sky, so that a proper comparison can be made.

4. Summary

Our results highlight the complex nature of optical/near-IR color selected EROs. The high resolution HST morphologies indicate that disks are the dominant constituent of the bright ($K < 20$ mag) ERO population selected with an ($I - K$) color greater than or equal to 4 magnitudes. Galaxies classified as spheroids, which can be considered comparable to passively evolving elliptical or S0 galaxies, and strongly interacting systems which may represent dusty starbursts, only contribute small fractions to the total ERO population. There are real differences in the surface densities of EROs selected by their ($R - K$) color as compared to the ($I - K$) samples, which may reflect a preferential selection of disks in I-band based ERO surveys and in any case complicates the comparison of various surveys and their interpretation. In addition, edge-on disk galaxies comprise a significant fraction of our ERO sample: 40% of the disks, or 28% of the full sample. Even small amounts of dust in this orientation could redden otherwise normal disk galaxies at lower redshift ($z < 1$) sufficiently to be included in the ERO samples. Our results imply that hierarchical merging and continuing accretion of gas still play an important and continuing role in the evolution of massive galaxies, even though most

of their stellar mass may already be in place by $z \sim 1$.

We thank Myungshin Im for helpful discussions about the MDS. This research was supported by the HST grant AR-08756 and the NASA Long Term Space Astrophysics program under the grant NAG5-10955. The MDS is based on observations with the NASA/ESA Hubble Space Telescope, obtained at the Space Telescope Science Institute, which is operated by the Association of Universities for Research in Astronomy, Inc., under NASA contract NAS5-26555.

REFERENCES

- Afonso, J., Mobasher, B., Chan, B., & Cram, L. 2001, *ApJ*, 559, L101
- Andreani, P., Cimatti, A., Röttgering, H., & Tilanus, R. 1999, *Ap&SS*, 266, 267
- Barger, A.J., Cowie, L.L., Trentham, N., Fulton, E., Hu, E.M., Songaila, A., & Hall, D. 1999, *AJ*, 117, 102
- Bertin, E. & Arnouts, S. 1996, *A&AS*, 117, 393
- Bruzual, G. & Charlot, S. 1996 ...
- Chapman, S.C., McCarthy, P.J., & Persson, S.E. 2000, *AJ*, 120, 1612
- Cimatti, A., Andreani, P., Röttgering, H., & Tilanus, R. 1998, *Nature*, 392, 895
- Cimatti, A., Villani, D., Pozzetti, L., & di Serego Alighieri, S. 2000, *MNRAS*, 318, 453
- Cimatti, A., Daddi, E., Mignoli, M., Pozzetti, L., Renzini, A., Zamorani, G., Broadhurst, T., Fontana, A., Saracco, P., Poli, F., Cristiani, S., D'Odorico, S., Giallongo, E., Gilmozzi, R., & Menci, N. 2002, *A&A*, 381, 68
- Couch, W.J., Barger, A.J., Smail, I., Ellis, R.S., & Sharples, R.M. 1998, *ApJ*, 497, 188
- Daddi, E., Cimatti, A., Pozzetti, L., Hoekstra, H., Röttgering, H.J.A., Renzini, A., Zamorani, G., & Mannucci, F. 2000, *A&A*, 361, 535
- Daddi, E., Cimatti, A. & Renzini, A. 2000, *A&A*, 362, L45

- Dey, A., Spinrad, H., & Dickinson, M. 1995, *ApJ*, 440, 515
- Dey, A., Graham, J.R., Ivison, R.J., Smail, I., Wright, G.S., & Liu, M.C. 1999, *ApJ*, 519, 610
- Djorgovski, S., Soifer, B. T., Pahre, M. A., Larkin, J. E., Smith, J. D., Neugebauer, G., Smail, I., Matthews, K., Hogg, D. W., Blandford, R. D., Cohen, J., Harrison, W., & Nelson, J. 1995, *ApJ*, 438, L13
- Dressler, A., Oemler, A.Jr., Couch, W.J., Smail, I., Ellis, R.S., Barger, A., Butcher, H., Poggianti, B.M., & Sharples, R.M. 1997, *ApJ*, 490, 577
- Eisenhardt, P. & Dickinson, M. 1992, *ApJ*, 399, L47
- Ellis, R.S., Santos, M.R., Kneib, J.-P., & Kuijken, K. 2001, *ApJ*, 560, L119
- Elston, R., Rieke, G. H., & Rieke, M. J. 1989, *ApJ*, 341, 80
- Elston, R., Rieke, M. J., & Rieke, G. H. 1988, *ApJ*, 331, L77
- Graham, J.R., Dey, A. 1996, *ApJ*, 471, 720
- Graham, J.R., Matthews, K., Soifer, B. T., Nelson, J. E., Harrison, W., Jernigan, J. G., Lin, S., Neugebauer, G., Smith, G., & Ziomkowski, C. 1994, *ApJ*, 420, L5
- Griffiths, R.E., Casertano, S., Ratnatunga, K.U., Neuschaefer, L.W., Ellis, R.S., Gilmore, G.F., Glazebrook, K., Santiago, B., Huchra, J.P., Windhorst, R.A., Pascarelle, S.M., Green, R.F., Illingworth, G.D., Koo, D.C., & Tyson, A.J. 1994, *ApJ*, 435, L19
- Hibbard, J.E. & Vacca, W.D. 1997, *AJ*, 114, 1741
- Holland, W.S., Robson, E.I., Gear, W.K., Cunningham, C.R., Lightfoot, J.F., Jenness, T., Ivison, R.J., Stevens, J.A., Ade, P.A.R., Griffin, M.J., Duncan, W.D., Murphy, J.A., & Naylor, D.A. 1999, *MNRAS*, 303, 659
- Hu, E. M. & Ridgeway, S. E. 1994, *AJ*, 107, 1303
- Im, M., Yamada, T., Tanaka, I., & Kajisawa, M. 2002, *ApJ*, 578, L19
- Kochanek, C.S., Pahre, M.A., Falco, E.E., Huchra, J.P., Mader, J., Jarrett, T.H., Chester, T., Cutri, R., & Schneider, S.E. 2001, *ApJ*, 560, 566
- Lawrence, C.R., Elston, R., Januzzi, B.T., & Turner, E.L. 1995, *AJ*, 110, 2570
- Liu, M.C., Dey, A., Graham, J.R., Bundy, K.A., Steidel, C.C., Adelberger, K., & Dickinson, M.E. 2000, *AJ*, 119, 2556
- Lubin, L.M., Postman, M., Oke, J.B., Ratnatunga, K.U., Gunn, J.E., Hoessel, J.G., & Schneider, D.P. 1998, *AJ*, 116, 584
- Mannucci, F., Pozzetti, L., Thompson, D., Oliva, E., Baffa, C., Comoretto, G., Gennari, S., & Lisi, F. 2002, *MNRAS*, 329, L57
- McCarthy, P. J., Persson, S. E., & West, S. C. 1992, *ApJ*, 386, 52
- McCarthy, P.J., Carlberg, R.G., Chen, H.-W., Marzke, R.O., Firth, A.E., Ellis, R.S., Persson, S.E., McMahon, R.G., Lahav, O., Wilson, J., Martini, P., Abraham, R.G., Sabbey, C.N., Oemler, A., Murphy, D.C., Somerville, R.S., Beckett, M.G., Lewis, J.R., & MacKay, C.D. 2001, *ApJ*, 560, L131
- Mohan, N.R., Cimatti, A., Röttgering, H.J.A., Andreani, P., Severgnini, P., Tilanus, R.P.J., Carilli, C.L., & Stanford, S.A. 2002, *A&A*, 383, 440
- Moriondo, G., Cimatti, A., Daddi, E. 2000, *A&A*, 364, 26
- Murphy, D., Persson, S.E., Pahre, M.A., Sivaramakrishnan, A., & Djorgovski, S.G. 1995, *PASP*, 107, 1234
- Odewahn, S.C., Windhorst, R.A., Driver, S.P., Keel, W.C. 1996, *ApJ*, 472, L13
- Persson, S. E., McCarthy, P. J., Dressler, A., Matthews, K. 1993, in *The Evolution of Galaxies and Their Environment*, ed. D. Hollenbeck et al., NASA Conference Publication #3190, p. 78
- Poggianti, B.M. & Wu, H. 2000, *ApJ*, 529, 157
- Pozzetti, L. & Mannucci, F. 2000, *MNRAS*, 317, L17

- Ratnatunga, K.U., Griffiths, R.E., Casertano, S., Neuschaefer, L.W., & Wyckoff, E.W. 1994, *AJ*, 108, 2362
- Ratnatunga, K., Griffiths & Ostrander, E. 1999, *AJ*, 118, 86
- Smail, I., Ivison, R.J., Blain, A.W., & Kneib, J.-P. 1998, *ApJ*, 507, L21
- Smail, I., Ivison, R.J., Kneib, J.-P., Cowie, L.L., Blain, A.W., Barger, A.J., Owen, F.N., & Morrison, G. 1999, *MNRAS*, 308, 1061
- Smith, G.P., Smail, I., Kneib, J.-P., Czoske, O., Ebeling, H., Edge, A.C., Pelló, R., Ivison, R.J., Packham, C., & Le Borgne, J.-F. 2002a, *MNRAS*, 330, 1
- Smith, G.P., Smail, I., Kneib, J.-P., Davis, C.J., Takamiya, M., Ebeling, H., & Czoske, O. 2002b, *MNRAS*, 333, L16
- Soifer, B. T., Matthews, K., Djorgovski, S., Larkin, J., Graham, J. R., Harrison, W., Jernigan, G., Lin, S., Nelson, J., Neugebauer, G., Smith, G., Smith, J. D., & Ziomkowski, C. 1994, *ApJ*, 420, L1
- Soifer, B.T., Matthews, K., Neugebauer, G., Armus, L., Cohen, J.G., Persson, S.E., & Smail, I. 1999, *AJ*, 118, 2065
- Thompson, D., Beckwith, S. V. W., Fockenbrock, R., Fried, J., Hippelein, H., Huang, J.-S., von Kuhlmann, B., Leinert, Ch., Meisenheimer, K., Phleps, S., Röser, H.-J., Thommes, E., & Wolf, C. 1999, *ApJ*, 523, 100
- Treu, T., Stiavelli, M., Casertano, S., Møller, P., & Bertin, G. 2002, *ApJ*, 564, L13
- Treu, T., Stiavelli, M., Walker, A.R., Williams, R.E., Baum, S.A., Bernstein, G., Blacker, B.S., Carollo, C.M., Casertano, S., Dickinson, M.E., Demello, D.F., Ferguson, H.C., Fruchter, A.S., Lucas, R.A., MacKenty, J., Madau, P., & Postman, M. 1998, *A&A*, 340, L10
- van Dokkum, P. & Stanford, A. 2001, *ApJ*, 562, L35

TABLE 1
OBSERVATIONS.

MDS Field	N_{ERO}	5σ K_s limit ^a	FWHM arcsec	Exp Time (s)		MDS Field	N_{ERO}	5σ K_s limit ^a	FWHM arcsec	Exp Time (s)	
				K_s	$F814W$					K_s	$F814W$
u2845i8	5	18.85	1.25	5400	16000	ufj00i2	3	19.02	1.37	4800	4200
u29g1i6	0	18.55	1.43	5400	6600	ug502i4	0	18.54	1.68	3750	1700
u29g3i6	0	18.71	1.68	4350	6600	ugi00i2	0	18.27	1.74	2700	4700
u2b15i6	2	18.62	1.62	4500	3600	ugk00i2	0	18.45	1.56	3750	5400
u2c41i8	0	18.85	1.56	6450	16800	uha01i3	0	18.97	1.68	6750	4200
u2c47i6	3	19.29	1.50	9000	12600	uhg00i2	1	19.25	1.62	9750	5600
u2c48i6	3	18.63	1.99	4500	12600	uho00i3	1	18.89	1.62	4500	4500
u2f1i5	2	18.77	1.68	4500	10500	uih00i2	0	18.58	1.87	4500	4200
u2fq1i5	14	18.67	1.25	4800	10500	uim03i3	4	19.07	1.56	7650	4000
u2fq2i6	1	18.58	1.37	5400	12600	ujh01i2	1	18.87	1.99	4500	4200
u2gk1i3	1	18.62	1.68	4500	4800	uko01i2	2	19.07	1.56	5850	4200
u2h91ic	2	18.80	1.37	5400	28800	ulj00i4	3	19.49	1.43	13050	5100
u2iy1i6	1	18.43	1.93	3750	6400	uo501i3	5	18.93	1.50	12450	6300
u2iy2i6	0	18.67	1.62	4500	6400	upj00i2	0	18.97	1.56	4500	4200
u2uj2i3	1	18.64	1.43	4350	3600	uqc00i2	2	18.64	1.25	5400	4200
u2uj7i3	2	18.71	1.68	3750	3600	uqc01i2	2	19.15	1.43	9150	7200
u2um1ia	0	18.72	1.37	3750	11000	uqg00i2	0	18.42	1.31	2700	3600
u2v12i5	0	18.22	1.99	3000	6700	uqj10i3	3	18.93	1.50	5250	4100
u2v14i5	0	18.62	1.25	4200	6700	uqk00i2	6	19.26	1.50	9000	2450
u2v15i5	0	18.34	1.62	2700	6700	uqk02i4	2	18.89	1.62	4500	6600
u2v16i5	1	19.07	1.56	10650	6700	uqk04i4	1	19.06	1.56	4500	4000
u2v18i5	1	18.72	1.87	4350	6700	uqk11i5	3	18.93	1.37	4350	3100
u2v19i5	2	18.73	1.99	4200	6700	uql00i2	1	18.78	2.12	6000	4200
u3063i6	1	18.95	1.37	4500	14400	uri01i3	0	18.59	1.99	4500	3000
u30h1i4	0	18.75	1.74	4500	5000	usa00i3	1	18.68	1.68	4500	6300
u30h2i4	0	19.07	1.56	4500	5300	usa02i3	0	18.62	1.37	4050	6300
ubb10i2	0	18.45	1.93	4200	5800	usc10i7	1	18.82	1.68	9050	4500
ubi02i2	3	19.30	1.68	8850	4700	usc12i4	2	18.58	1.31	5250	4135
ubm00i3	1	18.81	1.56	4500	5400	utb11i3	0	18.39	1.62	2700	9100
uci10i4	2	18.86	1.37	4950	10800	uub01i2	0	18.29	1.68	2700	2700
udh00i2	1	18.80	1.56	4500	3300	uuc04i6	2	18.72	1.62	7200	3900
udm00i2	0	18.69	1.74	4500	3000	uvm01i2	1	19.02	1.37	4500	4600
udm10i3	1	18.75	1.87	4500	5400	uwp00i3	1	18.61	1.99	4500	8400
uec00i2	4	18.48	1.37	2700	3000	ux400i4	2	18.69	1.50	4350	7500
ued01i2	0	18.53	1.37	2700	5600	uxn00i2	0	18.89	1.87	4500	2800
ueg00i3	0	18.60	1.37	2700	6300	uxs10i3	1	18.74	1.43	4500	6200
ueh02i2	3	18.42	1.62	2700	4200	uys00i2	1	18.61	1.87	4500	4600
uem00i5	0	18.69	2.06	4500	6600	uzk03i3	1	18.84	1.81	4500	4900
ufg00i2	5	18.65	1.74	4050	4700						

^aThe K_s limiting magnitudes are derived from the sky noise in the center of each infrared mosaic image, and are quoted as 5σ limits for a point source within an aperture diameter 2.5 times the FWHM of the seeing.

TABLE 2
EXTREMELY RED GALAXIES.

#	MDS ID#	Coordinates ^a		$K_s/I - K_s$	$K\sigma$	$I\sigma$	Morph.Class ^b		Comments ^c
		α	δ (J2000)				YT ^d	MDS	
1	ufg00#140	0:18:22.2928	+16:20:54.975	18.05 / 5.85	6.8	7.3	D	G	asym disk or 1fc
2	ufg00#070	0:18:29.1165	+16:20:56.226	18.27 / 5.23	7.2	5.8	DB	B	asym disk
3	ufg00#121	0:18:30.1373	+16:20:39.685	18.29 / 4.27	6.4	12.6	D	B	faint asym disk?
4	ufg00#044	0:18:31.2524	+16:20:43.706	17.68 / 4.16	9.4	33.4	B	B	mfc, merger?
5	ufg00#083	0:18:31.5131	+16:20:40.797	18.05 / 4.60	5.9	15.5	B	G	1fc + tail, merger?
6	uhg00#049	0:20:11.5736	+28:36:51.713	18.12 / 4.24	9.6	26.6	ID	DB	DB + lg tidal tail
7	udh00#057	0:45:02.1324	+10:34:42.958	18.58 / 4.05	5.6	13.1	D	B	faint disk
8	ueh02#120	0:53:35.3406	+12:49:29.408	18.28 / 4.15	5.8	16.5	D	D	asym, LSB
9	ueh02#063	0:53:35.6556	+12:49:50.997	17.43 / 4.82	11.4	29.7	B	BD	faint disk
10	ueh02#104	0:53:39.9393	+12:49:34.931	18.08 / 4.92	5.8	15.2	DB	B	asym or 1fc
11	ujh01#118	1:09:03.3016	+35:35:36.262	18.71 / 4.62	5.4	11.7	D	D	lg disk
12	ubi02#055	1:09:56.7526	-02:26:18.601	18.49 / 4.03	8.6	23.6	D	B	asym disk
13	ubi02#062	1:09:57.0151	-02:27:34.353	18.46 / 4.71	8.7	14.4	B	B	faint disk?
14	ubi02#013	1:10:00.4624	-02:27:37.273	17.04 / 4.18	28.8	99.9	B	S	stellar core + mfc, AGN?
15	uci10#013	1:24:40.8825	+03:50:45.704	17.57 / 4.17	15.5	99.9	B	BD	bright spheroid
16	uci10#051	1:24:45.9369	+03:51:19.209	18.62 / 4.02	5.3	18.6	ID	D	dbl nucl + mfc, merger
17	ubm00#093	2:01:50.2325	-11:41:14.232	18.29 / 4.30	7.6	27.3	DB	D	asym disk
18	ufj00#077	2:07:01.3073	+15:26:18.414	18.67 / 4.08	5.0	23.1	DB	DB	asym disk
19	ufj00#052	2:07:05.7003	+15:24:55.156	17.74 / 4.70	15.5	19.2	DB	B	lg LSB disk, asym nucl
20	ufj00#047	2:07:07.6300	+15:24:43.365	18.29 / 4.14	9.0	24.8	B	B	stellar core + 2fc, AGN?
21	u2c48#049	2:39:56.0682	-01:37:07.046	17.33 / 4.25	15.7	77.1	ID	D	merger, lg tidal tail?
22	u2c48#078	2:39:59.2569	-01:37:21.172	17.55 / 4.35	13.2	46.7	DB	DB	lg disk, dust/arms
23	u2c48#114	2:40:00.5682	-01:37:07.237	18.22 / 4.45	6.3	28.1	D	DB	face-on LSB disk or mfc
24	udm10#100	2:42:52.0311	-00:05:08.190	18.45 / 4.73	5.0	7.2	IU	G	spur or fc to disk
25	ulj00#053	2:43:50.2612	+37:17:53.956	18.49 / 4.34	11.7	15.0	DB	B	faint asym disk or 1fc
26	ulj00#219	2:43:50.3033	+37:17:23.852	19.12 / 5.72	7.0	2.7	D	D	v.faint LSB disk
27	ulj00#114	2:43:50.8212	+37:17:14.400	19.22 / 4.26	6.7	7.8	D	G	irr, asym
28	u2iy1#022	3:02:47.3464	+00:13:08.655	17.22 / 4.45	9.8	53.8	DB	DB	lg disk
29	u2v19#079	3:38:37.9233	-00:13:03.154	18.33 / 4.30	6.5	17.6	D	D	lg LSB disk
30	u2v19 ...	3:38:38.5961	-00:12:42.727	17.69 / 4.15	12.4	48.9	B	-	2 EROs (2''sep)
31	u2v18#036	3:41:09.5269	+00:00:18.660	17.90 / 4.43	7.7	42.9	B	BD	asym
32	uim03#102	3:55:31.1522	+09:44:47.822	18.60 / 4.04	7.7	15.0	DB	D	...
33	uim03#089	3:55:32.3447	+09:44:49.683	18.57 / 4.02	6.6	18.9	BD	B	faint disk?
34	uim03#100	3:55:32.8000	+09:44:47.262	18.34 / 4.51	7.6	12.7	BD	DB	asym
35	uim03#075	3:55:35.4355	+09:42:43.514	17.94 / 4.63	8.1	16.5	DB	DB	asym
36	u2f1#038	4:14:41.8303	+05:35:47.750	17.84 / 4.50	7.2	39.7	D	DB	asym, 1fc
37	u2f1#044	4:14:43.0621	+05:34:39.376	18.29 / 4.20	7.1	32.4	B	B	1fc
38	uho00#069	4:16:55.7078	-05:59:36.262	18.64 / 4.62	6.0	9.9	DB	DB	LSB disk
39	uko01#043	4:56:49.0888	+03:52:37.939	18.21 / 4.10	6.7	34.5	B	D	bright, resolved core
40	uko01#023	4:56:43.3215	+03:53:33.905	18.85 / 4.00	5.1	22.1	B	B	1fc
41	uqk11#019	7:24:41.3649	+60:29:37.564	17.07 / 4.08	9.0	83.0	D	BD	lg disk, asym, dust
42	uqk11#077	7:24:43.8276	+60:31:37.111	18.21 / 4.39	6.2	17.9	D	D	LSB disk or irr
43	uqk11#048	7:24:46.6626	+60:30:35.571	18.11 / 4.00	6.6	27.3	DB	DB	asym
44	uqj10#027	7:27:20.6173	+69:05:46.966	17.73 / 4.05	6.8	44.7	D	D	LSB disk, 1bc
45	uqj10#062	7:27:25.4097	+69:06:17.115	18.42 / 4.65	7.4	10.9	D	DB	LSB disk or irr
46	uqj10#080	7:27:42.9072	+69:06:50.422	18.46 / 5.27	5.1	17.3	D	D	asym
47	uqk02#042	7:41:25.8953	+65:06:02.339	18.55 / 4.01	6.0	14.4	DB	DB	asym or 1fc
48	uqk02#064	7:41:31.6545	+65:06:09.883	18.51 / 4.40	6.3	11.3	D	D	dbl nucl
49	uqk00#133	7:42:37.6428	+65:06:32.076	18.38 / 5.38	7.1	4.9	U	G	compact, asym
50	uql00#314	7:42:39.3423	+49:44:31.800	18.54 / 4.37	5.2	18.9	U	G	v.faint, LSB
51	uqk00#299	7:42:44.2458	+65:05:49.770	18.77 / 4.36	5.8	9.7	U	D	v.faint, asym
52	uqk00#096	7:42:44.6454	+65:05:49.863	18.71 / 4.12	6.3	12.0	D	D	LSB disk or irr
53	uqk00#066	7:42:49.2476	+65:05:06.184	18.77 / 4.21	5.1	11.4	D	D	LSB disk, asym or 1bc
54	uqk04#039	7:42:49.6767	+65:15:43.206	18.03 / 4.09	10.8	7.1	B	B	asym nucl
55	uqk00 ...	7:42:49.7006	+65:06:08.519	18.78 / 4.04	5.4	7.9	B	-	asym
56	uqk00#043	7:42:51.0075	+65:06:23.044	18.58 / 4.84	5.8	9.7	B	D	asym
57	u2gk1#190	8:30:48.3166	+65:51:12.636	18.22 / 4.99	6.1	4.7	DB	G	asym, 1bc, merger?
58	uvm01#194	9:39:31.7625	+41:33:09.070	18.85 / 4.57	5.6	7.4	DB	G	asym
59	u2c47#165	9:42:57.2880	+46:56:01.780	18.86 / 4.68	6.6	13.1	D	D	asym, dbl nucl or dust lane
60	u2c47#085	9:43:03.5351	+46:55:50.805	17.91 / 4.06	11.7	36.9	BD	DB	...
61	u2c47#134	9:43:08.0085	+46:56:21.209	18.54 / 4.43	8.4	21.7	D	D	asym, mfc
62	uwp00#051	10:02:26.2962	+28:50:00.903	18.03 / 4.79	7.2	22.6	DB	DB	asym, 2fc
63	uxs10#035	10:47:13.2802	+13:56:37.675	17.90 / 4.46	6.9	24.8	DB	B	faint disk, 1fc
64	uys00 ...	11:16:28.0883	+18:05:27.717	17.87 / 4.15	10.2	25.4	B	-	stellar core, AGN?

TABLE 2—*Continued*

#	MDS ID#	Coordinates ^a		$K_s/I - K_s$	$K\sigma$	$I\sigma$	Morph.Class ^b		Comments ^c
		α	δ				YT ^d	MDS	
65	u3063#511	11:40:29.4030	+66:07:58.555	18.86 / 6.05	5.2	2.6	D	D	LSB disk or irr
66	uzk03#086	12:10:31.1231	+39:28:46.905	18.19 / 4.07	8.5	17.3	DB	B	1fc
67	u2b15#029	13:33:35.2177	+16:50:11.271	18.33 / 4.07	5.4	34.5	BD	D	faint disk, mfc
68	u2b15#046	13:33:37.1951	+16:50:00.346	18.32 / 4.01	6.0	17.6	D	B	asym
69	u2uj2#164	13:59:48.8443	+62:31:47.959	18.21 / 4.12	6.3	22.6	DB	DB	LSB disk
70	u2uj7#082	13:59:54.7421	+62:28:35.463	18.14 / 4.20	6.5	9.6	DB	DB	...
71	u2uj7#171	14:00:07.8212	+62:28:51.163	18.65 / 4.53	5.1	11.8	U	B	compact, LSB
72	ux400 ...	15:19:39.4365	+23:52:37.885	18.60 / 4.11	5.1	28.1	DB	- ^e	lg asym disk + 1fc
73	ux400#055	15:19:40.7129	+23:52:39.488	18.25 / 4.16	6.7	32.4	BD	DB	asym disk
74	u2845#097	16:04:15.4230	+43:04:15.840	18.75 / 4.56	5.1	20.0	DB	B	lg asym disk
75	u2845#077	16:04:17.4446	+43:03:47.643	18.70 / 4.64	5.3	33.4	BD	B	1fc?
76	u2845#043	16:04:17.7243	+43:03:24.653	18.10 / 4.64	6.9	33.4	D	D	lg LSB disk, dust lane
77	u2845#089	16:04:21.3952	+43:04:35.810	18.32 / 4.57	8.1	28.1	DB	B	...
78	u2845#050	16:04:25.2398	+43:04:12.562	17.95 / 4.14	6.4	53.8	B	B	1bc
79	uuc04#095	17:55:22.4485	+48:10:14.906	17.66 / 4.50	12.0	23.1	DB	DB	asym LSB disk, 1bc, merger?
80	uuc04#044	16:24:15.3071	+48:09:37.509	17.89 / 4.14	6.2	32.4	DB	B	mfc, tidal tail?
81	usa00 ...	17:12:20.6910	+33:35:28.969	17.94 / 4.19	8.1	38.3	ID	- ^e	merger (poss barred sp?)
82	usc12#072	17:22:37.0496	+50:13:35.231	17.94 / 4.13	7.9	28.1	B	B	...
83	usc12#045	17:22:37.6296	+50:13:00.220	17.88 / 4.05	9.8	34.5	DB	DB	lg late type spiral
84	usc10#056	17:23:00.3707	+50:10:54.617	18.22 / 4.02	5.1	24.2	DB	B	1fc, arm
85	uo501#171	17:55:22.4072	+18:18:47.134	18.47 / 4.05	5.9	23.6	B	B	...
86	uo501#258	17:55:25.4940	+18:17:09.218	18.46 / 4.17	5.3	27.3	DB	DB	asym, 2bc
87	uo501#207	17:55:26.3237	+18:17:15.018	18.51 / 4.52	6.1	22.1	BD	D	1fc
88	uo501#123	17:55:27.6343	+18:18:55.559	17.97 / 4.09	10.9	31.4	B	B	...
89	uo501 ...	17:55:30.3430	+18:18:30.982	17.81 / 5.62	14.8	10.3	B	-	...
90	uqc01#065	18:07:04.9266	+45:44:13.350	18.57 / 4.09	8.3	20.4	BD	DB	...
91	uqc01#097	18:07:06.4575	+45:44:34.643	18.43 / 4.23	9.5	28.1	BD	B	faint disk, 1bc (lensed?)
92	uqc00#071	18:07:35.4057	+46:00:02.849	18.03 / 4.38	5.4	26.0	ID	D	irr or asym disk + dust
93	uqc00#111	18:07:43.7618	+45:59:45.389	18.26 / 4.60	6.7	18.2	B	B	faint disk?
94	u2fq1#130	21:53:30.6614	+17:41:45.643	17.91 / 4.05	5.1	48.9	D	D	dust lane
95	u2fq1#389	21:53:32.4668	+17:41:28.683	18.39 / 5.25	5.6	5.6	D	D	LSB
96	u2fq1#166	21:53:32.4989	+17:42:53.920	18.02 / 4.98	6.9	15.2	DB	BD	...
97	u2fq1#273	21:53:33.0947	+17:42:52.077	18.15 / 4.43	5.9	21.7	ID	D	1bc, poss merger
98	u2fq1#158	21:53:33.3712	+17:42:49.533	17.96 / 4.45	7.4	19.2	DB	DB	asym disk, 1fc
99	u2fq1#128	21:53:33.8187	+17:41:15.458	17.37 / 4.10	11.7	63.4	B	DB	asym nucl, mbc, merger?
100	u2fq1#184	21:53:33.8420	+17:43:01.576	18.13 / 4.59	7.2	22.1	DB	DB	...
101	u2fq1#095	21:53:34.0945	+17:42:40.723	16.77 / 5.02	26.6	53.8	DB	BD	lg disk, 2bc
102	u2fq1#416	21:53:34.5140	+17:43:05.921	18.53 / 5.01	5.0	7.7	U	G	asym, 1fc
103	u2fq1#107	21:53:38.5288	+17:42:18.217	17.17 / 4.24	14.6	59.8	B	B	faint disk?
104	u2fq1#085	21:53:38.6836	+17:41:07.398	17.04 / 4.29	13.2	42.9	BD	BD	bright S0/Sa?
105	u2fq1#115	21:53:38.8887	+17:42:25.657	17.86 / 4.31	11.6	30.5	B	B	...
106	u2fq1#099	21:53:39.1231	+17:42:25.960	17.51 / 4.17	16.2	59.8	D	DB	lg disk, asym
107	u2fq1#224	21:53:39.7393	+17:41:12.323	18.18 / 5.02	7.2	14.4	DB	B	...
108	u2v16 ...	22:17:35.4817	+00:17:34.004	18.82 / 4.60	5.9	10.8	U	-	nearby comp.
109	u2h91#034	22:17:35.8459	+00:13:51.524	17.70 / 4.27	8.8	67.4	DB	DB	lg disk, poss bar, 2fc ^f
110	u2h91#011	22:17:37.6791	+00:15:57.024	17.25 / 4.14	8.8	98.2	D	DB	lg asym disk; ^f
111	u2fq2 ...	22:47:09.9607	-02:05:57.959	17.58 / 4.34	10.9	38.3	D	-	lg disk w/knots, ^g
112	uec00#057	23:04:24.4209	+03:04:10.043	18.19 / 4.15	5.7	23.1	DB	DB	...
113	uec00#053	23:04:29.4158	+03:03:31.358	18.01 / 4.10	6.4	23.6	DB	BD	asym disk
114	uec00#080	23:04:30.4987	+03:04:43.728	18.07 / 4.20	6.7	14.6	D	D	LSB disk or irr
115	uec00#047	23:04:31.2224	+03:04:35.336	17.81 / 4.38	7.4	16.5	D	BD	asym, dust

^aCoordinates are in the format $00^h00^m00^s.00 \pm 00^o00'00''00$, derived from the HST world coordinate system.

^bMorphological classifications from this paper (YT) and the Medium Deep Survey (MDS). The primary classifications are (B) Bulge, (BD) Bulge-dominated disk, (DB) Disk with a bulge, and (D) Disk. See text for further details.

^cAbbreviations in the comments: lg=large; asym=asymmetric; 1fc, 2fc, mfc=[1,2,multiple] faint companions; 1bc, 2bc, mbc=[1,2,multiple] bright companions; LSB=Low Surface Brightness; AGN=Active Galactic Nucleus; dbl=double; nucl=nucleus; v=very; irr=irregular; poss=possible; comp=companion.

^dItalicized entries indicate that the galaxy appears sufficiently inclined that dust may make a significant contribution to the integrated color.

^eThe MDS incorrectly fits these galaxies with multiple components

^fu2h91#034 is SSA22 Hawaii#77 at $z=1.02$; u2h91#011 is SSA22 Hawaii#64 at $z=0.653$

^gThis object could drop off the sample as some light from the extended disk is lost in the gap between WFPC2 CCDs.

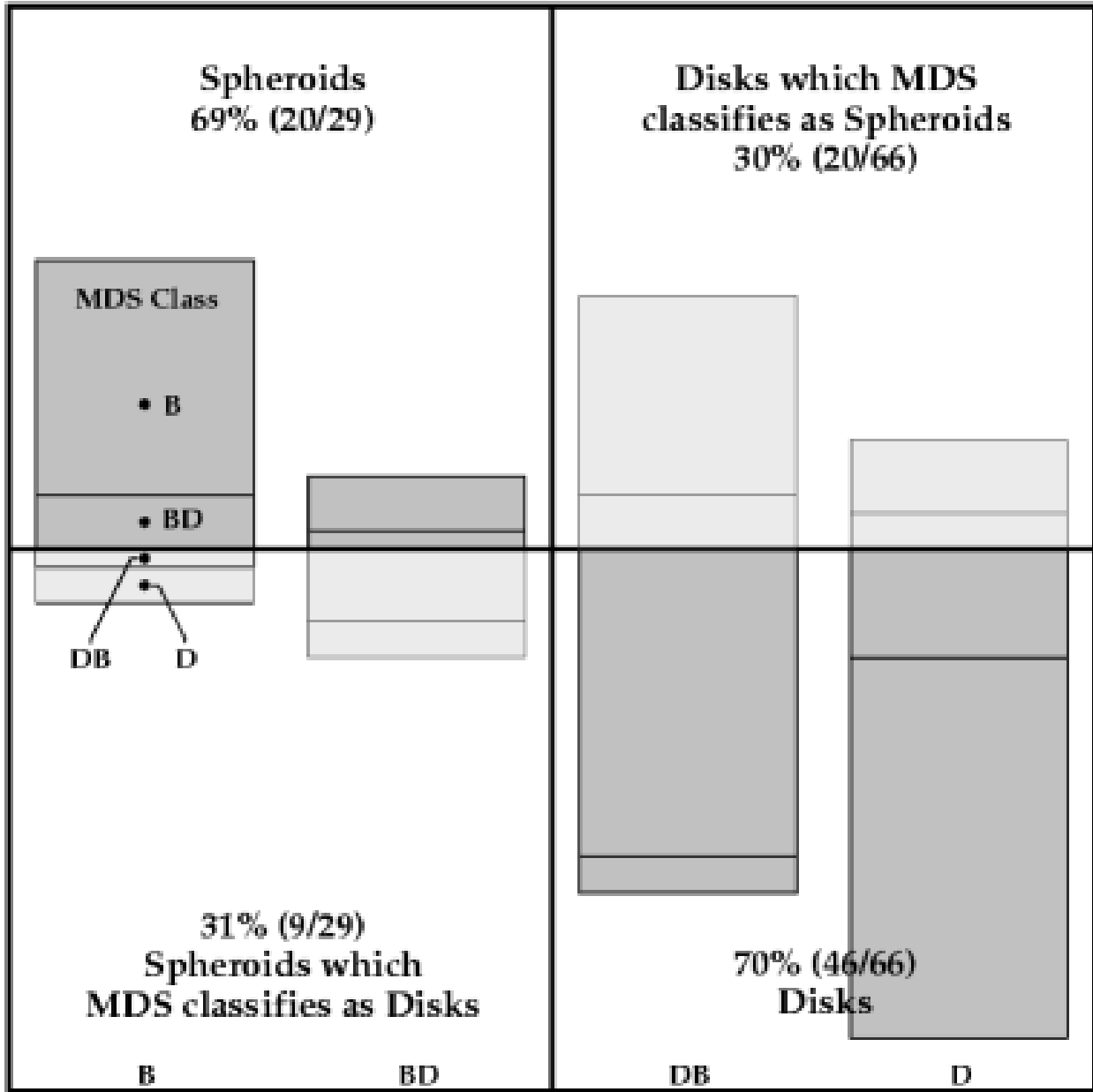


Fig. 10.— Full-resolution HST/WFPC2 F814W images of all 115 EROs. Each image is $8''$ square, rotated from the default HST orientation to have north up and east to the left. The numbers in each subimage correspond to the object numbers in Table 2.